ADVANCED FUNCTIONAL MATERIALS
www.afm-journal.de

Materials Views
www.MaterialsViews.com

FULL PAPER

Graphene-Based Mesoporous SnO_2 with Enhanced Electrochemical Performance for Lithium-Ion Batteries

Sheng Yang, Wenbo Yue, Jia Zhu, Yu Ren, and Xiaojing Yang**

Graphene-based metal oxides generally show outstanding electrochemical performance due to the superior properties of graphene. However, the aggregation of active metal oxide nanoparticles on the graphene surface may result in a capacity fading and poor cycle performance. Here, a mesostructured graphene-based SnO_2 composite is prepared through in situ growth of SnO_2 particles on the graphene surface using cetyltrimethylammonium bromide as the structure-directing agent. This novel mesoporous composite inherits the advantages of graphene nanosheets and mesoporous materials and exhibits higher reversible capacity, better cycle performance, and better rate capability compared to pure mesoporous SnO_2 and graphene-based nonporous SnO_2. It is concluded that the synergetic effect between graphene and mesostructure benefits the improvement of the electrochemical properties of the hybrid composites. This facile method may offer an attractive alternative approach for preparation of the graphene-based mesoporous composites as high-performance electrodes for lithium-ion batteries.

1. Introduction

Lithium-ion batteries (LIBs) have been widely used in portable electronic devices (e.g,. laptops) due to their superior properties such as high energy density, long cycle life, no memory effect and environmental friendliness. Many metals and metal oxides have been intensively studied as potential high-performance electrodes for LIBs due to their high theoretical capacities, natural abundance and low cost. For instance, SnO_2 has a high theoretical capacity of 782 mA h g^{-1}, much higher than that of the conventional graphite anode (≈370 mA h g^{-1}).[1] Notwithstanding, SnO_2 anodes are lack of practical use due to the severe volume change and the aggregation of Sn clusters during cycles, which result in a rapid capacity fading and the end of the cycle life.[2] Some methods have been developed to alleviate the volume changes and to protect the electrode from pulverization such as controlled fabrication of nanoscale materials (e.g., SnO_2 nanowires),[3] hollow materials (e.g., SnO_2 hollow spheres),[4] and carbon-based composites (e.g., carbon-coated SnO_2).[5] Recently, a novel two-dimensional carbon matrix, graphene, has attracted tremendous attention and is preferable to replace other carbon matrices (e.g., graphite or carbon nanotube) for supporting metal and metal oxides due to its excellent properties such as high electrical conductivities, unique mechanical properties and large specific surface areas.[6–8] In the past five years, the preparation and morphological control of graphene-based metal oxides (or metals) have been thoroughly explored for a range of applications. For instance, graphene-based Pt (or Pd) composites exhibit desirable catalytic activity and stability towards alcohol oxidation and can be used as anodes in direct alcohol fuel cells.[9,10] Graphene-based or graphene-encapsulated metal oxides (or metals) also show excellent electrochemical performances as electrode materials for LIBs.[11–13] The graphene substrate itself can be contributory to the improved electrochemical performance because it may enhance the electronic conductivity of the overall electrode,[11] benefit the high dispersion of nanoscale particles,[12] and effectively buffer the strain from the volume variation during lithiation and delithiation processes.[13] As one of the most promising negative electrode materials in LIBs, SnO_2 particles were also decorated on graphene surface through several strategies to improve its electrochemical property.[14–16] Particularly, it is recently reported that SnO_2 with controlled morphology and crystallinity can be formed on graphene nanosheets by the atomic layer deposition (ALD) technique. The graphene-amorphous SnO_2 showed higher specific capacity and better cycling stability in comparison with the graphene-crystalline SnO_2 because amorphous SnO_2 was more effective in overcoming electrochemical and mechanical degradation.[14] However, compared to metal or metal oxide electrodes, the theoretical capacity of graphene is much lower (≈744 mA h g^{-1} for LiC_3 and ≈372 mA h g^{-1} for LiC_6), which leads to the decrease in the reversible capacity of the graphene-based composite, especially in the cases of low content of metal oxides (or metals).[17,18] On the other hand, the high level of metal oxides accompanied with the partial aggregation of particles may also result in the rapid capacity loss and poor cycle performance.[19]

The mesoporous metal oxides as novel nanostructured materials not only deliver high reversible capacity due to their large surface areas, but also exhibit good cycle performance and rate

---

S. Yang, Prof. W. B. Yue, Prof. J. Zhu, Prof. X. J. Yang
Beijing Key Laboratory of Energy Conversion
and Storage Materials
College of Chemistry
Beijing Normal University
Beijing 100875, P. R. China
E-mail: wbyue@bnu.edu.cn; yang.xiaojing@bnu.edu.cn

Dr. Y. Ren
National Institute of Clean-and-low-carbon Energy
Beijing, 102209, P. R. China

DOI: 10.1002/adfm.201203286

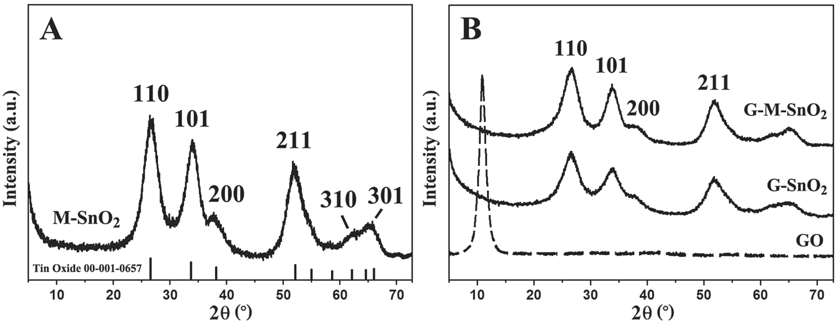

Figure 1. XRD patterns of A, M-SnO$_2$ and B, GO, G-SnO$_2$, G-M-SnO$_2$, respectively.

capability because the uniform pores also act as a buffer against the volume variation and provide favorable structural stability during cycles.[20–23] It has been reported that SnO$_2$ particles with mesoporous structure exhibit enhanced electrochemical properties in comparison with its bulk counterpart.[24,25] However, the capacity fading still occurs in the porous samples after several cycles because the mesopores may partially collapse during the charge-discharge process.[26,27] In situ growth of mesoporous SnO$_2$ on the carbon substrate (e.g., carbon nanotube) is beneficial for stabilizing the mesostructure during cycles.[28] This gives a hint that graphene-based mesoporous SnO$_2$ may exhibit high reversible capacity and good cycle stability even for those with high content of SnO$_2$. Herein we describe a facile solvothermal strategy for preparation of graphene-based SnO$_2$ with mesoporous structure (G-M-SnO$_2$) by using cetyltrimethylammonium bromide (CTAB) as the structure-directing agent. In addition, to study the influence of mesostructure and graphene substrate on the electrochemical performance of SnO$_2$ electrodes, mesoporous SnO$_2$ (M-SnO$_2$) and graphene-base nonporous SnO$_2$ (G-SnO$_2$) were also synthesized by selective adding graphene oxides (GO) and CTAB. The as-synthesized G-M-SnO$_2$ possesses large surface area, good electrical conductivity and stable pore structure, which renders it as an advanced material in the fields of electrical and optical devices, catalysts, gas sensing, and energy storage.

2. Results and Discussion

2.1. Morphology and Structural Characterization

The crystalline phases of M-SnO$_2$, G-SnO$_2$ and G-M-SnO$_2$ samples were firstly identified by X-ray diffraction (XRD). All the XRD peaks for M-SnO$_2$ (**Figure 1**A) are indexable to the tetragonal SnO$_2$ structure (space group $P4_2/mnm$, a = 0.4738 and c = 0.3187 nm), indicating the formation of pure SnO$_2$ crystals. In Figure 1B, the GO exhibited only one peak centered at ca. 11°, corresponding to a basal spacing of ≈0.8 nm. Owing to the introduction of various oxygen-containing functionalities (e.g., carboxyl, hydroxyl or epoxy) between layers, the basal spacing was greatly expanded from 0.335 nm (pristine graphite) to 0.779 nm (GO).[29] Interestingly, the graphene-based SnO$_2$ composite, either G-SnO$_2$ or G-M-SnO$_2$, has similar XRD pattern corresponding to the SnO$_2$ structure without the appearance of the 11° peak for GO. It may be attributed to the reduction of GO, which would be confirmed by other measurements below. The conventional stacking peak of graphene nanosheets, usually located at ca. 26°, is also absent in the patterns. This implies that the SnO$_2$ particles were formed on the both surfaces of graphene nanosheets, preventing the graphene nanosheets from restacking. The particle size calculated from broad XRD peaks corresponded to 3–3.5 nm, suggesting the formation of SnO$_2$ nanoparticles or mesoporous wall consisting of SnO$_2$ nanocrystallines.

The reduction of GO in the composites were further investigated by FT-IR and XPS. **Figure 2**A shows the FT-IR spectra of GO, G-SnO$_2$ and G-M-SnO$_2$ samples. The absorption bands centered at 1734, 1374, 1227, 1061 and 1624 cm^{-1} are present in the FT-IR spectrum of GO, corresponding to the stretching vibration of C=O (carboxyl or carbonyl), O−H (carboxyl or absorbed water), C−OH (hydroxyl) and C−O (epoxy or alkoxy).[29] In the FT-IR spectra of G-SnO$_2$ and G-M-SnO$_2$, the C−O band disappears and the intensity of O−H and C=O bands become much weaker in comparison with that of C=C band, indicating the removal of most oxygen functionalities. The absorption band at ≈621 cm^{-1} can be assigned to the vibration of Sn-O-Sn, confirming the presence of SnO$_2$ in composites.[30] Figure 2B shows a survey XPS spectrum from G-M-SnO$_2$ sample and three elements (C, O and Sn) were distinguished. Moreover, the Sn 3d$_{3/2}$ and Sn 3d$_{5/2}$ peaks depicted in the fine spectrum of Sn 3d (the inset of Figure 2B) also confirm the formation of SnO$_2$-containing composite.[30] Figure 2C and 2D show the fine spectra of C 1s from G-SnO$_2$ and G-M-SnO$_2$ samples. The C 1s peak can be further divided into four peaks, which is located at 284.6, 286.6, 287.6, 288.9 eV and assigned to C−C (sp^2 C), C−O, C=O, O−C=O groups, respectively.[29] These C 1s peaks related to the oxidized groups are noticeably weak, suggesting the complete reduction of GO, which is in good agreement with the FT-IR result. Thus, the G-SnO$_2$ and G-M-SnO$_2$ samples are indeed composed of graphene and SnO$_2$ crystals. TGA was used to determine the contents of SnO$_2$ in G-SnO$_2$ and G-M-SnO$_2$ specimens (Supporting Information Figure S1). The results show that there is not much difference between the mass percentages of SnO$_2$, ≈79.5 wt% for G-SnO$_2$ and ≈78.8 wt% for G-M-SnO$_2$.

The morphology and structure of SnO$_2$ samples were elucidated by TEM. Supporting Information Figure S2A shows a representative TEM image of the as-prepared M-SnO$_2$ and the disordered wormhole-like pores can be observed. The HRTEM image of M-SnO$_2$ (Supporting Information Figure S2B) indicates that the mesoporous walls are composed of connected nanocrystalline SnO$_2$ sized 3–4 nm in diameter. The porosity of M-SnO$_2$ was also investigated using nitrogen adsorption/desorption techniques. The isotherm of M-SnO$_2$ (Supporting Information Figure S3A) shows a typical type IV curve with a type H1 hysteresis loop, confirming the mesoporous feature of M-SnO$_2$. The BJH pore size distribution curve (Supporting Information Figure S3B) gives a pore diameter of 3.5 nm,[28] which is consistent with the TEM observation. The TEM images

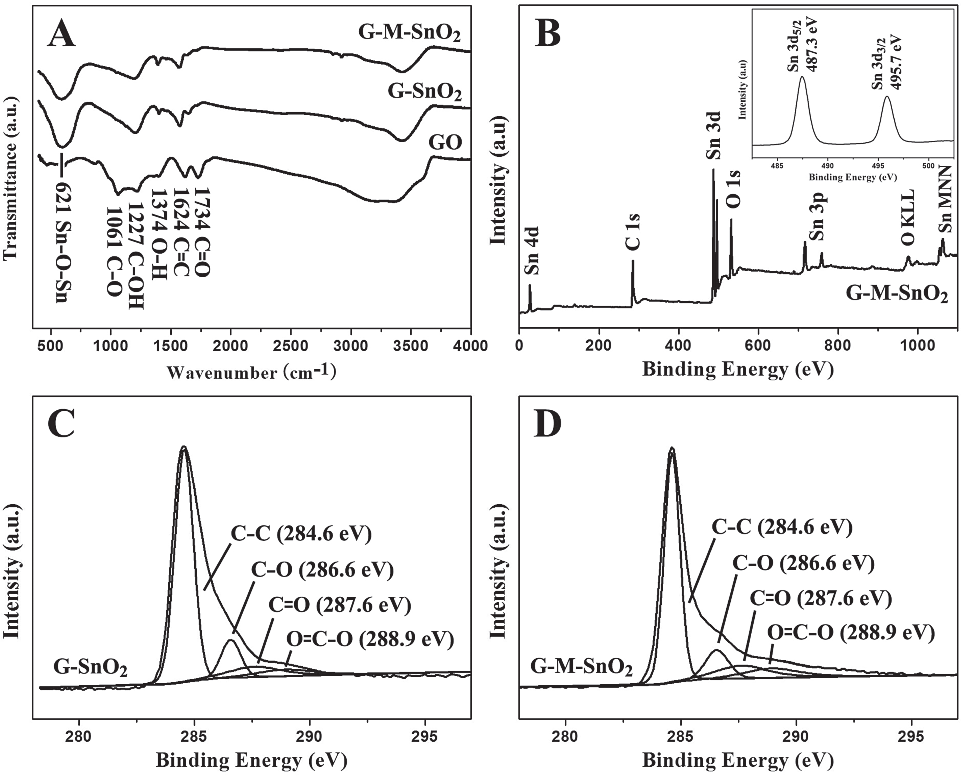

Figure 2. A) FT-IR spectra of GO, G-SnO$_2$ and G-M-SnO$_2$. B) Survey XPS spectrum of G-M-SnO$_2$. The inset is the fine spectrum of Sn 3d. C,D) C1s XPS spectra of G-SnO$_2$ and G-M-SnO$_2$, respectively.

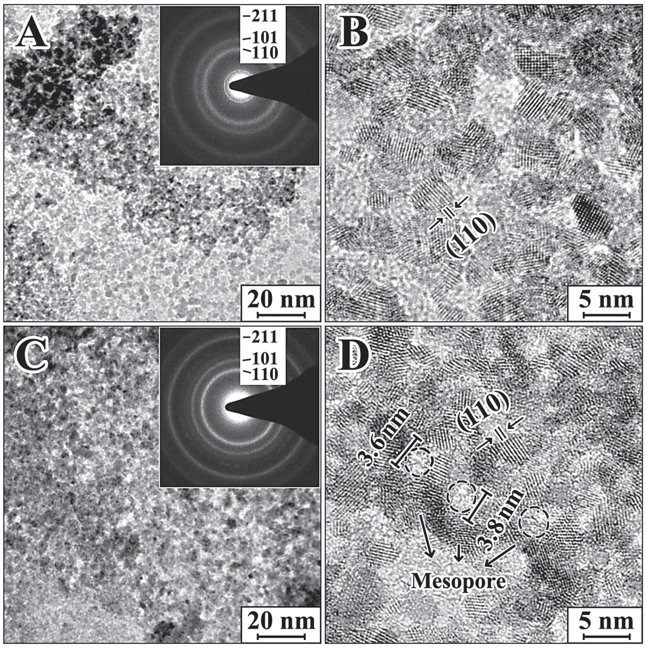

Figure 3. TEM and HRTEM images of A,B) G-SnO$_2$ and C,D) G-M-SnO$_2$, respectively. The insets of (A,C) are the SAED patterns of G-SnO$_2$ and G-M-SnO$_2$.

of the porous and nonporous graphene-based SnO$_2$ are shown in **Figure 3**. For the G-SnO$_2$ sample (Figure 3A), many SnO$_2$ particles pervasively overlaid on the surface of graphene, resulting in the high loading of SnO$_2$ (≈79.5%). It is noted that the aggregation of SnO$_2$ particles is inevitable for G-SnO$_2$ sample, but does not occur in G-M-SnO$_2$ sample (Figure 3C) with a similar content of SnO$_2$ (≈78.8%). HRTEM images of G-SnO$_2$ and G-M-SnO$_2$ samples could provide more details about structure, particle size and crystal lattice. It is obvious that, for G-SnO$_2$ sample, the nanoparticles with size ranging from 3–4 nm appear randomly on graphene surface (Figure 3B) and exhibit well-defined lattice spacing of ≈0.332 nm, corresponding to the (110) planes of SnO$_2$ crystal. In addition, the aggregation of SnO$_2$ nanoparticles can also be observed at the top right of the HRTEM image. On the contrary, the mesoporous SnO$_2$ particles consisting of SnO$_2$ nanocrystalline in the wall were formed on graphene surface (Figure 3D), and no evident SnO$_2$ agglomerates can be detected due to the use of CTAB. The mesopore have a diameter of 3.6–3.8 nm and the wall thickness is about 3 nm. The d-spacings of the marked fringes in the HRTEM image is ca. 0.333 nm, agreeing well with the d-spacing of the (110) plane of SnO$_2$ crystal. As shown in the insets of Figure 3A and 3C, the SAED patterns of G-SnO$_2$ and G-M-SnO$_2$ from large areas can also be indexed to the tetragonal SnO$_2$ structure, which are consistent with the HRTEM results. The morphology and structure of G-M-SnO$_2$ was further confirmed by SEM. The low-magnification SEM image of G-M-SnO$_2$ reveals the large 2D graphene nanosheets, on which SnO$_2$ nanoparticles were uniformly deposited (Supporting Information Figure S4A). Supporting Information Figure S4B represents a high-magnification SEM image of G-M-SnO$_2$. The SnO$_2$ layers with disordered 4–5 nm pore arrays can be observed distinctly on the

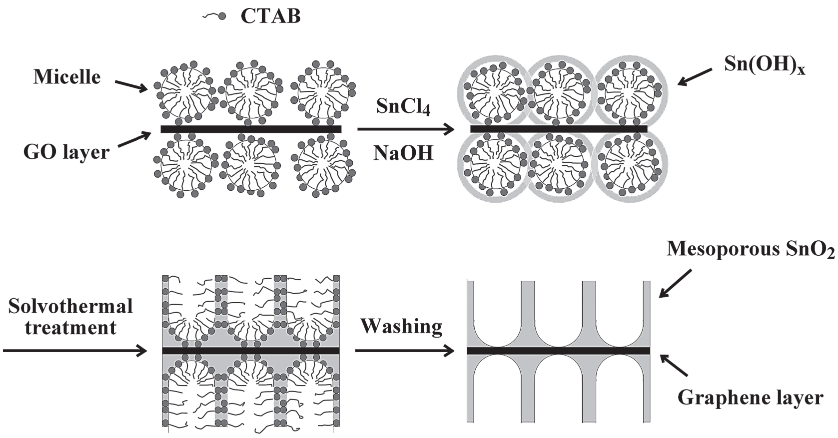

Figure 4. Schematic mechanism for the formation of G-M-SnO_2 sample.

surface of graphene nanosheets. Because the mesoporous walls are observable distinguishably, these small pores were formed through the growth of SnO_2 crystals around the CTAB template rather than through a random aggregation of its nanoparticles. Some large pores (or gaps) with different diameters may be attributed to the exposed areas of graphene substrate that was not occupied by SnO_2 or CTAB. A possible mechanism is proposed to explain the formation of G-M-SnO_2 (**Figure 4**). The single layers of GO in solution were negatively charged under a highly basic environment, which could strongly adsorb the CTA^+ ions through electrostatic interactions and then initialize the formation of micelle assemblies.[31,32] Subsequently, Sn^{4+} ions were added afterward into the GO-CTA^+ solution and rapidly reacted with OH^- to form negatively charged $Sn(OH)_x$ at the interface of the micelles. Since some micelles were close to one another, further polymerization of $Sn(OH)_x$ leads to linkage of neighboring micelles on the GO surface, and may induce a structural transformation of spherical micelles to cylindrical ones, yielding a mesoporous SnO_2 crystalline on GO surface after solvothermal treatment. Simultaneously, GO was reduced to graphene under the solvothermal condition. The mesopores were finally formed after removing CTAB surfactants by thorough washing with warm ethanol.

The N_2 adsorption/desorption isotherms of G-SnO_2 and G-M-SnO_2 were also studied. In **Figure 5**A, a type IIb curve with a H3 hysteresis loop at the relative pressure of 0.5-1 (P/P_0) is indicative of non-rigid slit-shaped pores; while in Figure 5C, a type IV curve with a H1 hysteresis loop at the relative pressure of 0.5-0.8 is indicative of large channel-like pores in a narrow size range. This difference in the isotherms clearly indicates the difference between these two samples. Namely, the pores of G-SnO_2 sample were formed by random aggregation of SnO_2 particles and the pores are various in size (Figure 5B), whereas the pores of G-M-SnO_2 sample were derived from mesoporous materials with a uniform diameter of 3.8 nm (Figure 5D), which is similar with M-SnO_2. The specific surface area of G-M-SnO_2 measured by the BET method is 251.7 m^2/g, which is much larger than that of G-SnO_2 (164.3 m^2/g), and even larger than that of M-SnO_2 (184.7 m^2/g), implying the high dispersion of porous SnO_2 decorated on graphene nanosheets.

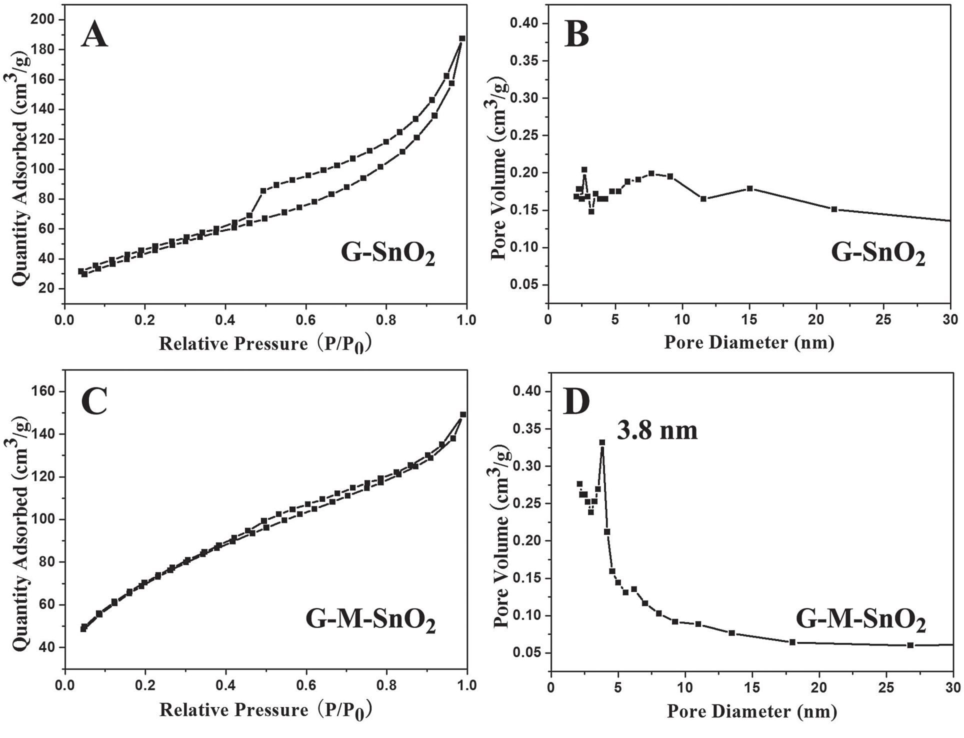

Figure 5. A,C) N_2 adsorption/desorption isotherms measured at 77 K from G-SnO_2 and G-M-SnO_2. B,D) the corresponding pore size distribution.

2.2. Electrochemical Testing

The electrochemical performances of M-SnO_2, G-SnO_2 and G-M-SnO_2 samples were evaluated by galvanostatic measurements. **Figure 6**A shows the first and second cycle charge–discharge voltage profiles for the three samples at a constant current density of 0.1 C (1 C = 782 mA g^{-1}). Two slope regions can be identified in the discharge process of the first cycle, which are in good agreement with those of SnO_2-based anodes,[18,19,24,25] indicating the same electrochemical pathway. Namely, the high plateaus around 0.8 V could be assigned to the transformation of $SnO_2 + Li^+$ to $Sn + Li_2O$, and the low plateaus around 0.3 V could be attributed to the formation of Li_xSn alloy. However, in case of the graphene-based SnO_2 (either G-SnO_2 or G-M-SnO_2), the higher plateau nearly disappears after the first cycle, indicating that only the conversion of Sn to Li_xSn alloy occurrs in the following cycles. Therefore, compared to pure SnO_2, graphene-based SnO_2 showed a higher Coulombic efficiency, ca. 64.0% for G-SnO_2 and 69.4% for G-M-SnO_2 at the first cycle, thereafter above 91.2% for G-SnO_2 and 95.3% for G-M-SnO_2 at the following cycles. The first discharge capacity of G-M-SnO_2 is ca. 1595.6 mA h g^{-1}, much higher than that of M-SnO_2 (1310.7 mA h g^{-1}) and G-SnO_2 (1526.9 mA h g^{-1}). This increased discharge capacity may be attributed to the high electrical conductivity of graphene substrate and the high specific surface area of the mesostructured SnO_2 on graphene. Figure 6B shows the cycle performances of the three samples at a current density of 0.1 C. M-SnO_2 exhibited stable reversible capacities at the initial five cycles, and the capacity decreased dramatically after five cycles, possibly resulting from the collapse of mesopores. In contrast, G-SnO_2 showed much better cycle performance and higher reversible capacities, e.g., ≈507.9 mA h g^{-1} after 50 cycles, which is still higher than the theoretical capacity of graphite (≈370 mA h g^{-1}). The structure of SnO_2 particles is more stable on graphene, which may effectively buffer the strain from the volume variation and restrain the aggregation of Sn clusters. As expected, graphene substrate may also stabilize the mesostructure of SnO_2, leading to the further improvement of the electrochemical properties of G-M-SnO_2. Compared to G-SnO_2, G-M-SnO_2 exhibited superior and more stable reversible capacities, e.g., 847.5 mA h g^{-1} after 50 cycles, even higher than the theoretical capacity of SnO_2 (≈782 mA h g^{-1}). The excess capacities could be attributed to the formation of the SEI film on the surface of active materials, which are also observed for other graphene-based metal oxides (e.g., Co_3O_4).[26] The cycle performances of reported SnO_2 nanowire,[3] SnO_2 hollow sphere,[4] carbon-coated SnO_2[5] and graphene-based SnO_2[15,16] are also listed in Supporting Information Table S1 to compare their electrochemical properties with that of graphene-based mesoporous SnO_2. Although the current density and the cycle number were slightly different, G-M-SnO_2 still exhibits much higher capacity after 50 cycles.

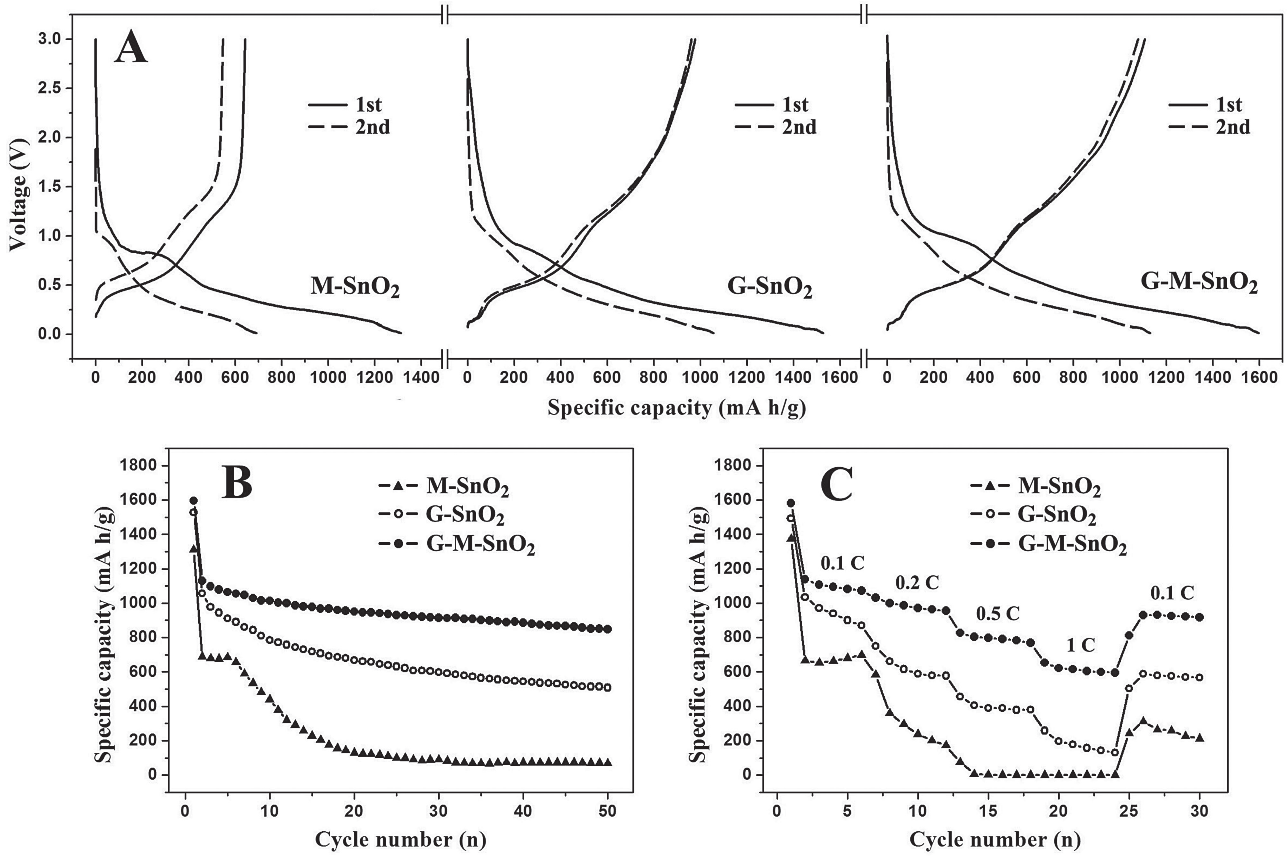

Figure 6. A) the first and second cycle charge–discharge curves for M-SnO_2, G-SnO_2 and G-M-SnO_2 at 0.1 C in the voltage range 0.01–3.0 V. B,C) The discharge capacities as a function of cycle numbers for the three samples at 0.1 C and 0.1–1 C.

Figure 6C shows the rate capabilities of the three samples evaluated by measurements of them at different current densities. It is striking to note that the capacity of M-SnO_2 decreased rapidly with the increase of the current density, while G-SnO_2 showed better rate capability than M-SnO_2. Reasonably, G-M-SnO_2 delivers excellent reversible capacity, which is as high as ≈621.5 mA h g^{-1} even at a high current density of 782 mA g^{-1}. Additionally, a capacity of ≈916.9 mA h g^{-1} was retained after 30 cycles when the current density recovered to 0.1 C, also implying their good cycling stabilities. The better rate capability can be attributed to the enhanced electronic and ionic conductivity of the electrode induced by the graphene substrate and the mesostructure of SnO_2. The electrochemical impedance spectra (EIS) of M-SnO_2, G-SnO_2 and G-M-SnO_2 (Supporting Information Figure S5) were also carried out to gain insight into the superior electrochemical behavior of G-M-SnO_2. The Nyquist plots of the three samples showed two partially overlapped semicircles in the high and middle frequency range, corresponding to the migration of the Li^+ ions through the SEI film (R_f) and the charge-transfer impedance (R_{ct}) on electrode/electrolyte interface, and a sloping line in the low frequency range, corresponding to the diffusion of the Li^+ ions in the bulk of the electrode (Z_w). In the high frequency range, the radius of the semicircle for M-SnO_2 was much larger than that for G-SnO_2 or G-M-SnO_2. In the middle frequency range, the radius of the semicircle for M-SnO_2 increased sharply with the number of cycles, whereas that for G-SnO_2 increased slightly. Apparently, the R_{ct} values of G-SnO_2 and G-M-SnO_2 were much smaller than that of M-SnO_2 because the graphene substrate can improve the electronic conductivity of the overall electrode. The R_{ct} value of G-M-SnO_2 did not change much before 5 cycles. It is 30.4 Ω after 10 cycles, even smaller than that of G-SnO_2 after 10 cycles (53.7 Ω), indicating the faster transfer rate of Li^+ ions in G-M-SnO_2. A probable explanation is that the porosity of SnO_2 enhances the electrode/electrolyte interface and shortens the Li^+ ion diffusion length in the G-M-SnO_2.[21]

It was reported previously that SnO_2 particles tend to aggregate into Sn clusters during cycling, leading to a large volume variation and the collapse of mesopores, while the dispersed SnO_2 on graphene surface provided free space to accommodate the volume expansion.[24,25] The morphology and structure of M-SnO_2, G-SnO_2 and G-M-SnO_2 after 50 cycles were observed by TEM. Large agglomerates instead of mesoporous particles were clearly demonstrated in the TEM image of M-SnO_2 (Supporting Information Figure S6A), implying the collapse of mesoporous structure and aggregation of Sn particles during cycles. However, the agglomeration was considerably reduced and some separated Sn nanoparticles were observable in G-SnO_2 sample (Supporting Information Figure S6B), suggesting that graphene nanosheets probably slowed down the rate of particle agglomeration. In the TEM image of G-M-SnO_2 (Supporting Information Figure S6C), the mesostructured Sn particles were still preserved (white arrows), suggesting that graphene stabilizes the mesostructure during cycles. Consequently, graphene-based mesoporous metal oxides have following advantages: i) As an ideal substrate to disperse mesoporous metal oxides, graphene not only enhances the electronic conductivity of the electrode and buffers the strain from the volume expansion, but also restrains the aggregation of tin clusters and maintains the mesostructure during cycles; ii) The mesopore of metal oxides offers large specific surface area which accommodates more Li^+ ions, leading to a high reversible capacity and provides free space to accommodate the volume expansion during alloying and dealloying processes. The results of preliminary experiments on the growth of mesoporous SnO_2 on graphene nanosheets can provide a new possibility of preparation of other graphene-based mesoporous metal oxides.

3. Conclusions

We described a facile strategy for the preparation of graphene-based mesoporous SnO_2 through in situ growth of SnO_2 around CTAB template on graphene surface under solvothermal conditions. This novel mesoporous composite exhibits a great improvement in electrochemical performance as an anode material for LIBs, such as higher capacity, better cycle performance and rate capability in comparison with pure mesoporous SnO_2 and graphene-based nonporous SnO_2. The superior electrochemical property can be attributed to the presence of graphene substrate and the mesostructure as well as the synergetic effect between graphene and mesostructure. Namely, on the surface of graphene, the formation of mesoporous structure, or controlled growth of the SnO_2 crystals, can avoid the aggregation, especially as a high loading of SnO_2 is desired, while the graphene substrate can take the role of restraining the collapse of the mesostructure against cycling. This controllable growth-on-graphene approach may offer an effective technique for preparation of other graphene-based mesoporous metal oxides that can be applied in the fields of electrical and optical devices, catalysts, gas sensing, and energy storage.

4. Experimental Section

Preparation of Graphene Oxide: Graphene oxide was synthesized from natural graphite powders by a modified Hummer's method.[33] In brief, graphite powder (5 g, average size 20 µm, apparent density 0.05 g cm^{-3}) and $NaNO_3$ (5 g) were added into H_2SO_4 (230 mL, 98%) under stirring in an ice bath. $KMnO_4$ (30 g) was slowly added to the mixture under stirring for 15 min at below 5 °C. The mixture was then heated at 35 °C for 30 min. Subsequently, distilled water (460 mL) was slowly introduced into the above mixture, followed by stirring the mixture at 98 °C for more than 15 min. The mixture was further diluted with distilled water (1400 mL) and the reaction was terminated by adding H_2O_2 (25 mL, 30%). Meanwhile, the color of the solution turned from dark brown to bright yellow. The resulting mixture was filtered and washed with distilled water several times to remove residual acids and salts. As-prepared GO was dispersed in water by ultrasonication for 30 min, followed by a low-speed centrifugation to get rid of any aggregated GO nanosheets.

Synthesis of Graphene-Based Mesoporous Tin Oxides: Graphene-based mesoporous SnO_2 was synthesized by using CTAB as soft template. In brief, graphene oxide (0.10 g) was dissolved in mixed solvent of ethanol and water (60 mL, volume ratio 5:1) by ultrasoncation for 0.5–1 h to form a homogeneous dispersion. Subsequently, CTAB (1.10 g) was added into the mixture with vigorous stirring for uniform dispersion before the addition of NaOH (0.004 mol) and $SnCl_4$ (0.002 mol). After stirring for 10 min, the mixture was transferred into a 80 mL Teflon-lined stainless steel autoclave and maintained at 160 °C for 12 h. The resulting dark-grey precipitate was collected by centrifugation, washed thoroughly with warm ethanol and water and then dried at 60 °C in a vacuum box overnight. The mesoporous SnO_2 and the graphene-based nonporous

SnO_2 were synthesized by using a similar method, but without adding GO or CTAB. The resulting products were denoted as M-SnO_2, G-SnO_2 and G-M-SnO_2, respectively.

Materials Characterizations: Specimens were initially characterized using XRD on a Phillips X'pert Pro MPD diffractometer with Cu K_α radiation. A Quantachrome NOVA 2000e sorption analyzer was used to examine the N_2 adsorption and desorption properties of specimens at liquid nitrogen temperature. The Fourier transform infrared (FT-IR) spectra were recorded on a Nicolet-380 Fourier-transform infrared spectrometer in the range of 400–4000 cm^{-1} and X-ray photoelectron (XPS) spectra were recorded on a Shimadzu Axis Ultra spectrometer with an Mg K_α = 1253.6 eV excitation source. The thermogravimetric analysis (TGA) was performed on a NETZSCH STA 409 PC/PG thermal analyzer and carried out in air at a heating rate of 5 °C min^{-1}. Further characterization was performed by using transmission electron microscopy (TEM) and high-resolution TEM (HRTEM) on a JEOL JEM-2011 electron microscope operated at 200 kV, and scanning electron microscope (SEM) on a JEOL Ltd. JSM-6700F electron microscope at an accelerating voltage of 1 kV.

Electrochemical Measurements: For electrochemical characterisation, the composite electrodes were fabricated by mixing the active materials, acetylene black and polyvinylidene difluoride (PVDF) dissolved in *N*-methyl-2-pyrrolidine (NMP) in a weight ratio of 70:15:15. The mixed slurry was pressed onto a copper foil and dried at 110 °C in vacuum for 24 h. Cell assembly was carried out in an Ar-filled glove box. The electrolyte was 1 M solution of $LiPF_6$ in EC:DEC:DMC with volume ratio 1:1:1. Electrochemical performances were measured with a CR2032-type coin cell with lithium metal as the negative electrode. The galvanostatic charge–discharge performance was measured with a LAND test system at room temperature, and the voltage range was from 0.01 to 3.0 V (versus Li/Li^+), with a constant current of 0.1–1 C (1 C = 782 mA g^{-1}). The electrochemical impedance spectroscopy (EIS) was carried out in the frequency range from 100 kHz to 10 mHz on a Princeton PARSTAT 4000 electrochemical station.

Supporting Information

Supporting Information is available from the Wiley Online Library or from the author.

Acknowledgements

This work is financially supported by National Natural Science Foundation of China (20903013, 21101014, 21273022 and 51272030) and Beijing Municipal Natural Science Foundation (2112022).

Received: November 9, 2012
Revised: December 26, 2012

---

[1] Y. Idota, T. Kubota, A. Matsufuji, Y. Maekawa, T. Miyasaka, *Science* **1997**, *276*, 1395.
[2] C. Kim, M. Noh, M. Choi, J. Cho, B. Park, *Chem. Mater.* **2005**, *17*, 3297.
[3] M. S. Park, G. X. Wang, Y. M. Kang, D. Wexler, S. X. Dou, H. K. Liu, *Angew. Chem. Int. Ed.* **2007**, *46*, 750.
[4] S. J. Ding, X. W. Lou, *Nanoscale* **2011**, *3*, 3586.
[5] Y. Li, S. M. Zhu, Q. L. Liu, J. J. Gu, Z. P. Guo, Z. X. Chen, C. L. Feng, D. Zhang, W.-J. Monn, *J. Mater. Chem.* **2012**, *22*, 2766.
[6] A. K. Geim, K. S. Novoselov, *Nat. Mater.* **2007**, *6*, 183.
[7] K. S. Novoselov, A. K. Geim, S. V. Morozov, D. Jiang, M. I. Katsnelson, I. V. Grigorieva, S. V. Dubonos, A. A. Firsov, *Nature* **2005**, *438*, 197.
[8] A. Fasolino, J. H. Los, M. I. Katsnelson, *Nat. Mater.* **2007**, *6*, 858.
[9] J.-D. Qiu, G.-C. Wang, R.-P. Liang, X.-H. Xia, H.-W. Yu, *J. Phys. Chem. C* **2011**, *115*, 15639.
[10] Y. C. Zhao, L. Zhan, J. N. Tian, S. L. Nie, Z. Ning, *Electrochim. Acta* **2011**, *56*, 1967.
[11] H. L. Wang, L. F. Cui, Y. Yang, H. S. Casalongue, J. T. Robinson, Y. Y. Liang, Y. Cui, H. J. Dai, *J. Am. Chem. Soc.* **2010**, *132*, 13978.
[12] L. W. Ji, Z. K. Tan, T. Kuykendall, E. J. An, Y. B. Fu, V. Battaglia, Y. G. Zhang, *Energy Environ. Sci.* **2011**, *4*, 3611.
[13] S. B. Yang, X. L. Feng, S. Ivanovici, K. Müllen, *Angew. Chem. Int. Ed.* **2010**, *49*, 8408.
[14] X. F. Li, X. B. Meng, J. Liu, D. S. Geng, Y. Zhang, M. N. Banis, Y. L. Li, J. L. Yang, R. Y. Li, X. L. Sun, M. Cai, M. W. Verbrugge, *Adv. Funct. Mater.* **2012**, *22*, 1647.
[15] X. D. Huang, X. F. Zhou, L. Zhou, K. Qian, Y. H. Wang, Z. P. Liu, C. Z. Yu, *ChemPhysChem* **2011**, *12*, 278.
[16] J. F. Liang, W. Wei, D. Zhong, Q. L. Yang, L. D. Li, L. Guo, *ACS Appl. Mater. Interfaces* **2012**, *4*, 454.
[17] G. X. Wang, B. Wang, X. L. Wang, J. Park, S. X. Dou, H. Ahnb, K. Kim, *J. Mater. Chem.* **2009**, *19*, 8378.
[18] S.-M. Paek, E. Yoo, I. Honma, *Nano Lett.* **2009**, *9*, 72.
[19] S. J. Ding, D. Y. Luan, F. Y. C. Boey, J. S. Chen, X. W. Lou, *Chem. Commun.* **2011**, *47*, 7155.
[20] T. Brezesinski, J. Wang, R. Senter, K. Brezesinski, B. Dunn, S. H. Tolbert, *ACS Nano* **2010**, *4*, 967.
[21] Z. Z. Lin, W. B. Yue, D. Z. Huang, J. Y. Hu, X. Y. Zhang, Z.-Y. Yuan, X. J. Yang, *RSC Adv.* **2012**, *2*, 1794.
[22] W. B. Yan, T. Ayvazian, J. Kim, Y. Liu, K. C. Donavan, W. D. Xing, Y. G. Yang, *ACS Nano* **2011**, *5*, 8275.
[23] H. S. Liu, Z. H. Bi, X.-G. Sun, R. R. Unocic, M. P. Paranthaman, S. Dai, G. M. Brown, *Adv. Mater.* **2011**, *23*, 3450.
[24] H. Kim, J. Cho, *J. Mater. Chem.* **2008**, *18*, 771.
[25] K. Shiva, H. B. Rajendra, K. S. Subrahmanyam, A. J. Bhattacharyya, C. N. R. Rao, *Chem. Eur. J.* **2012**, *18*, 4489.
[26] W. B. Yue, Z. Z. Lin, S. H. Jiang, X. J. Yang, *J. Mater. Chem.* **2012**, *22*, 16318.
[27] X. L. Yang, K. C. Fan, Y. H. Zhu, J. H. Shen, X. Jiang, P. Zhao, C. Z. Li, *J. Mater. Chem.* **2012**, *22*, 17278.
[28] Z. H. Wen, Q. Wang, Q. Zhang, J. H. Li, *Adv. Funct. Mater.* **2007**, *17*, 2772.
[29] S. Yang, W. B. Yue, D. Z. Huang, C. F. Chen, H. Lin, X. J. Yang, *RSC Adv.* **2012**, *2*, 8827.
[30] Y. M. Li, X. J. Lv, J. Lu, J. H. Li, *J. Phys. Chem. C* **2010**, *114*, 21770.
[31] Z.-M. Wang, W. D. Wang, N. Coombs, N. Soheilnia, G. A. Ozin, *ACS Nano* **2010**, *4*, 7437.
[32] Z. G. Teng, G. F. Zheng, Y. Q. Dou, W. Li, C.-Y. Mou, X. H. Zhang, A. M. Asiri, D. Y. Zhao, *Angew. Chem. Int. Ed.* **2012**, *124*, 2215.
[33] W. S. Hummers, R. E. Offeman, *J. Am. Chem. Soc.* **1958**, *80*, 1339.